Tuning of exchange constants and magnetic anisotropy for terahertz antiferromagnetic resonance frequencies in cation-doped NiO

Kenji Nawa,[1,2,*] Andi Gumarilang,[1] Takahiro Moriyama,[3,4] and Kohji Nakamura[1]

[1] *Graduate School of Engineering, Mie University, Tsu, Mie 514-8507, Japan*

[2] *Research Center for Magnetic and Spintronic Materials, National Institute for Materials Science (NIMS), Tsukuba, Ibaraki 305-0047, Japan*

[3] *Department of Materials Physics, Nagoya University, Chikusa, Nagoya 464-8603, Japan*

[4] *PRESTO, Japan Science and Technology Agency, Kawaguchi, Saitama 322-0012, Japan*

(Received 15 September 2023; revised 8 February 2024; accepted 27 February 2024; published 20 March 2024)

Advances in communication technology have moved carrier frequencies to the terahertz (THz) regime where the conventional microwave technologies and materials cannot work as their physical properties no longer respond to such frequencies. Antiferromagnets are materials whose magnetic properties respond and interact with THz-frequency electromagnetic waves. Phenomenologically, the response frequency is readily determined by the exchange energy and the magnetic anisotropy. In this paper, we revisit the antiferromagnetic resonance frequency of NiO, an archetypical antiferromagnetic material, and study the effect of cation doping (such as Li, Na, Be, Mg, Mn, Fe, and Zn) on its resonance frequency by first-principles calculations. The cation-dependent tunings of the exchange constant and magnetic anisotropy are demonstrated, with the resonance frequency varying from a minimum of 0.77 THz by Li doping to a maximum of 1.60 THz by Fe doping, referenced to a value of 1.20 THz obtained for pure NiO. Our findings encourage exploring of antiferromagnetic materials for future THz spintronic applications.

DOI: 10.1103/PhysRevApplied.21.034040

I. INTRODUCTION

Recent vigorous experimental and theoretical studies have revealed that, against the stereotypical belief that antiferromagnets are useless [1], they are actually a prime material for advancing spintronics technology [2]. For example, antiferromagnets can be used in the implementation of ultrahigh-density and high-speed magnetic memories by exploiting their intrinsic magnetic properties, i.e., no net magnetization and ultrafast spin dynamics along with various spintronic effects such as magnetoresistance [3–6] and spin-torque effect [7–10].

An interesting feature of antiferromagnets is their potential application as terahertz (THz)-frequency magnetic material. This is because their magnetic resonance typically occurs in the THz-frequency range, making them useful for next-generation communication technologies [11–13]. The antiferromagnetic resonance frequency is given phenomenologically as [14,15]

$$\omega_r = \gamma\sqrt{2H_{\mathrm{E}}H_{\mathrm{A}}}, \tag{1}$$

where $\gamma = 1.76 \times 10^{11}$ T^{-1} s^{-1} is the gyromagnetic ratio, H_{E} is an exchange field, and H_{A} is a magnetic anisotropy field. Typical values of H_{E} (approximately 1000 T) and H_{A} (approximately 1 T) make ω_r in the order of THz. In practical applications, it is desired that ω_r is tunable. Very recently, Moriyama *et al.* experimentally investigated the antiferromagnetic resonance of NiO by using THz transmission measurement and found that the value of ω_r can be modulated when NiO is doped with cations (Li^+, Mg^{2+}, and Mn^{2+}) in the 0.7–1.1 THz frequency range, where the variation of ω_r depends on the cation composition and most significantly on the cation species [16]. Ohkoshi *et al.* and Namai *et al.* also reported that a hematite ε-Fe_2O_3 exhibits a relatively low frequency of approximately 0.2 THz when doped with Ga [17] and Rh [18] cations. Wider tunability has been demonstrated in α-Fe_2O_3 with cation dopants in 0.21–0.95 THz frequency range by utilizing a characteristic variation of ω_r, which is associated with the magnetic phase transition temperature, often called Morin temperature [19].

These pioneering experiments demonstrated the wide tunability of resonance frequency in antiferromagnetic insulators doped with cations [16–19]. It was also reported that the resonance linewidths, characterizing the magnetic damping, can be modulated by intrinsic and extrinsic mechanisms in mono- and polycrystallinities [20] and by the interfacial effect [21]. A magneto-optical measurement for ultrathin film of yttrium iron garnet have observed that

*nawa@elec.mie-u.ac.jp

 © 2024 American Physical Society

even for the same sample, the extrinsic contribution to the linewidth varies depending on the orientation of the sample, namely Faraday geometry and Voigt geometry [22]. In Eq. (1), the value of ω_r depends on H_E and H_A, where doping impurity may affect either H_E or H_A, or both. Despite $H_E \gg H_A$, these effective fields contribute equally to the ω_r value since both are square rooted. For example, in Ref. [16], ω_r decreases as the composition of Mn dopants in NiO increases. This is due to the decrease in H_A. When NiO is doped with Li and Mg, ω_r decreases due to the decrease in both H_E and H_A. However, there is a lack of theoretical understanding regarding the impact of dopants on H_E and H_A, despite being very useful for establishing a guide of controlling ω_r based on theoretical principles.

In this paper, we theoretically investigate cation doping effects on ω_r in typical antiferromagnetic NiO. The exchange constant and the magnetic anisotropy in pure (nondoped) and cation-doped NiO are calculated from first-principles calculations, and the effective fields H_E and H_A are derived. The magnetic anisotropy is obtained from the sum of the anisotropy caused by the magnetic dipole-dipole interaction (MDIA) and the magnetocrystalline anisotropy (MCA). The cation dopants of *s* elements (Li^+, Na^+, Be^{2+}, and Mg^{2+}) and 3*d* elements (Mn^{2+}, Fe^{2+}, and Zn^{2+}) are considered, and the chemical tendency of ω_r is discussed. The calculations show that, in pure NiO, ω_r lies in the THz-frequency range, which is attributed to the large contribution of H_E due to the superexchange interaction via Ni-O-Ni. Three different mechanisms are presented, which modulate H_E and H_A from those in pure NiO. The exchange constants related to H_E are varied by doping monovalent *s*-element cations (Li^+ and Na^+). A change in the magnetic anisotropy related to H_A is induced by the MCA when doping with Fe and by the MDIA when doping Mn. The former yields the highest ω_r (1.60 THz) in this study, whereas the latter weakly affects ω_r. The comprehensive analysis presented in this work provides an insight into the frequency control of antiferromagnetic resonance and thus opens an avenue for alternative spintronic applications that utilizes ultrafast spin dynamics.

II. MODEL AND METHOD

Pure NiO is modeled using a rock-salt (RS) structure employing a $2 \times 2 \times 2$ supercell, where the three lattice vectors are represented by arrows in Fig. 1. The unit cell consists of eight Ni and eight O atoms. A dopant cation *X* is considered as an *s* element (Li^+, Na^+, Be^{2+}, and Mg^{2+}) or 3*d* element (Mn^{2+}, Fe^{2+}, and Zn^{2+}). In the unit cell of cation-doped NiO, one Ni atom is substituted by dopant *X*; hence, the dopant composition corresponds to 12.5%, i.e., $X_{0.125}Ni_{0.875}O$ in the chemical formula, which is referred to as *X*-doped NiO hereafter. The experimental value of 4.195 Å is used as the lattice constant of pure NiO, and all *X*-doped NiO systems are fixed to this value.

Density-functional-theory (DFT) calculations were performed using the full-potential linearized augmented plane-wave (FLAPW) method [23–25] with generalized gradient approximation (GGA) [26]. Since NiO is known as a strongly correlated electron system, the DFT+*U* method is employed within the atomic limit approximation [27], and the following effective on-site Coulomb

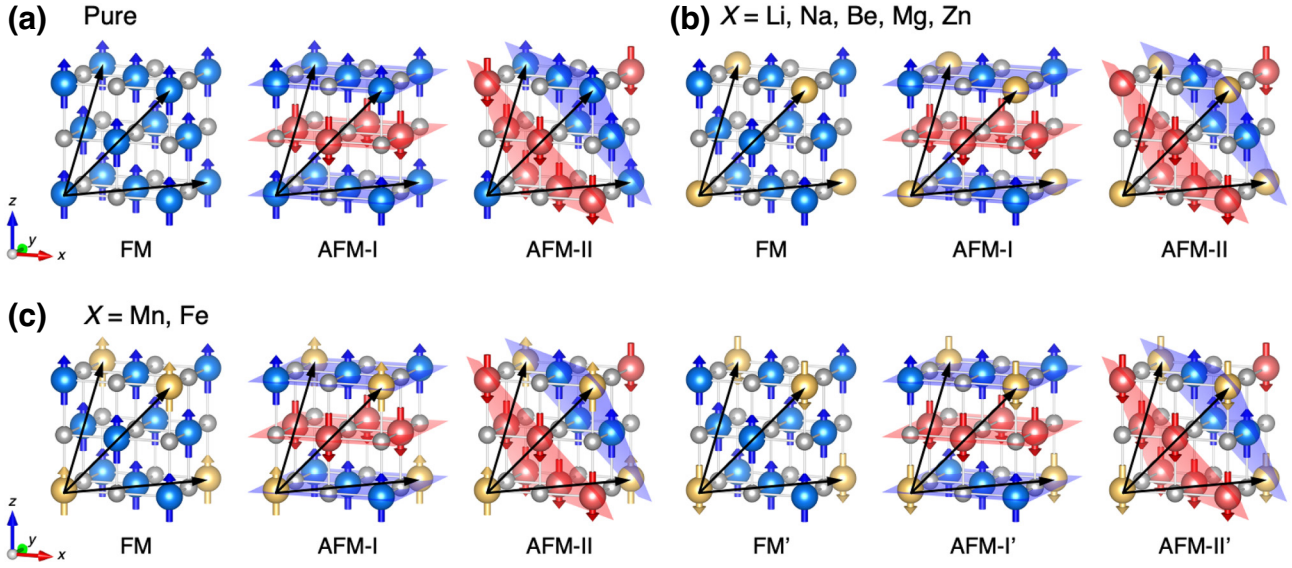

FIG. 1. Magnetic configurations considered in this study for (a) pure NiO and *X*-doped NiO with (b) *X* = Li, Na, Be, Mg, and Zn and (c) *X* = Mn and Fe. See the main text for details of each magnetic configuration. Circles indicate Ni with opposite magnetization directions (blue and red), O (gray), and dopant *X* (yellow). The spin direction of Ni cations is given as a guide to the eye and not the actual magnetization direction in the unit cell. The lattice vectors are shown in black.

TABLE I. Parameters used in the calculations, R_{MT} (in a_{B} unit), $\ell_{\max}$, and U_{eff} (in eV unit), for each atom.

	R_{MT} (a_{B})	$\ell_{\max}$	U_{eff} (eV)
Li	1.50	6	–
Na	2.00	6	–
Be	1.60	6	–
Mg	2.00	6	–
O	1.40	6	–
Mn	2.20	8	5.88
Fe	2.20	8	6.51
Ni	2.20	8	7.52
Zn	2.20	8	8.06

interaction parameter $U_{\mathrm{eff}} = U - J$ (where U and J are the Coulomb and exchange interactions, respectively) are derived using a linear-response approach [28]: $U_{\mathrm{eff}} = 5.88, 6.51, 7.52$, and 8.06 eV for Mn, Fe, Ni, and Zn, respectively, as listed in Table I. These values are obtained from the $X_{0.125}Ni_{0.875}O$ composition. The LAPW basis set has a cutoff of $|\mathbf{k} + \mathbf{G}| \leq 3.9$ a.u.$^{-1}$. The muffin-tin (MT) sphere radius R_{MT} and the angular momentum expansion $\ell_{\max}$ are also presented in Table I. Self-consistent field (SCF) calculations are performed using $15 \times 15 \times 15$ **k**-point sampling, and the atomic positions are relaxed [29] with a convergence criterion for the atomic force, 0.005 htr/Å, for all models.

The exchange constants are obtained by employing a total energy approach with a Heisenberg spin Hamiltonian, $H = -\sum_{i,j} J_{ij}\mathbf{S}_i \cdot \mathbf{S}_j$, where J_{ij} is the exchange constant between sites i and j, and $\mathbf{S}_i$ ($\mathbf{S}_j$) is a local magnetic moment at site i (j). In this approach, the total energies of multiple magnetic configurations are calculated by the DFT+U, and they are fitted to the Heisenberg model. For pure NiO, we consider exchange interactions J_1 and J_2 between first- and second-nearest neighbors Ni-Ni sites. As shown in Fig. 1(a), three magnetic configurations, ferromagnetic (FM), antiferromagnetic along [001] (AFM-I), and antiferromagnetic along [111] (AFM-II), are considered. The total energies of these configurations can be formulated as follows:

$$\begin{aligned} E_{\mathrm{FM}} &= E_0 - 48J_1S - 24J_2S, \\ E_{\mathrm{AFM\text{-}I}} &= E_0 + 16J_1S - 24J_2S, \\ E_{\mathrm{AFM\text{-}II}} &= E_0 + 24J_2S, \end{aligned} \tag{2}$$

where E_0 corresponds to the contribution of the nonmagnetic part in the system and S is given as $S = \mathbf{S}_{\mathrm{Ni}} \cdot \mathbf{S}_{\mathrm{Ni}}$. $|\mathbf{S}_{\mathrm{Ni}}|$ is assumed to be 1. Once the total energies are obtained from SCF calculations, J_1 and J_2 can be calculated using linear algebra.

When pure NiO is doped with a nonmagnetic X (Li, Na, Be, Mg, and Zn) [Fig. 1(b)], the exchange interaction between Ni and X sites becomes negligible, and the total energies can be formulated as follows:

$$\begin{aligned} E_{\mathrm{FM}} &= E_0 - 36J_1S - 18J_2S, \\ E_{\mathrm{AFM\text{-}I}} &= E_0 + 12J_1S - 18J_2S, \\ E_{\mathrm{AFM\text{-}II}} &= E_0 + 18J_2S. \end{aligned} \tag{3}$$

In contrast, for dopant X of magnetic cations (Fe and Mn), additional exchange interactions J_1' and J_2' appear for the first- and second-nearest neighbors between Ni and X sites; thus, three additional magnetic structures FM′, AFM-I′, and AFM-II′ are considered, where magnetization at the dopant site is flipped in relation to magnetizations in the FM, AFM-I, and AFM-II, respectively [Fig. 1(c)]. The exchange constants can be obtained from the following total energy equations:

$$\begin{aligned} E_{\mathrm{FM}} &= E_0 - 36J_1S - 18J_2S - 12J_1'S' - 6J_2'S', \\ E_{\mathrm{AFM\text{-}I}} &= E_0 + 12J_1S - 18J_2S + 4J_1'S' - 6J_2'S', \\ E_{\mathrm{AFM\text{-}II}} &= E_0 + 18J_2S + 6J_2'S', \\ E_{\mathrm{FM'}} &= E_0 - 36J_1S - 18J_2S + 12J_1'S' + 6J_2'S', \\ E_{\mathrm{AFM\text{-}I'}} &= E_0 + 12J_1S - 18J_2S - 4J_1'S' + 6J_2'S', \\ E_{\mathrm{AFM\text{-}II'}} &= E_0 + 18J_2S - 6J_2'S', \end{aligned} \tag{4}$$

where $S' = \mathbf{S}_{\mathrm{Ni}} \cdot \mathbf{S}_X$. Here, $|\mathbf{S}_X|$ is assumed to be 5/2 and 2 for X = Mn and Fe, respectively. Five unknown variables (J_1, J_2, J_1', J_2', and E_0) are obtained by fitting to the above six equations using the least-squares method.

Both the MCA and MDIA contribute to the magnetic anisotropy, and the magnetic anisotropy energy is given as $E_{\mathrm{MA}} = E_{\mathrm{MCA}} + E_{\mathrm{MDIA}}$. The MCA and MDIA energies are evaluated using

$$E_\alpha = E_\alpha^{[11\bar{2}]} - E_\alpha^{[111]}, \tag{5}$$

where α stands for MCA or MDIA, and $E_\alpha^{[11\bar{2}]}$ and $E_\alpha^{[111]}$ are the total energies of systems with a magnetization orientation along $[11\bar{2}]$ and [111] directions, respectively. The E_{MCA} is obtained using the force theorem [30,31]. The E_{MDIA} is obtained using the classical magnetic dipole-dipole interaction model, which straightforwardly sums long-range lattice interactions up to 400 Å [32]. The magnetic anisotropy and the exchange constants are evaluated using $31 \times 31 \times 31$ **k**-point sampling, confirming the convergence with respect to inadequate numerical fluctuations.

III. RESULTS AND DISCUSSION

A. Exchange constant

For pure NiO, the total-energy calculations showed that the AFM-II structure is a magnetic ground state and the energies of the FM and AFM-I structures are higher by

TABLE II. Total energy difference (in meV/cell) for different magnetic configurations (FM, AFM-I, AFM-II, FM′, AFM-I′, and AFM-II′) and magnetic ground state for X-doped NiO.

	dopant X	FM	AFM-I	AFM-II	FM′	AFM-I′	AFM-II′	Ground state
Nondoped	···	552	596	0	···	···	···	AFM-II
s elements	Li^{+}	161	179	0	···	···	···	AFM-II
	Na^{+}	321	339	0	···	···	···	AFM-II
	Be^{2+}	405	439	0	···	···	···	AFM-II
	Mg^{2+}	420	459	0	···	···	···	AFM-II
3d elements	Mn^{2+}	536	589	0	422	451	131	AFM-II
	Fe^{2+}	415	556	0	404	416	78	AFM-II
	Zn^{2+}	412	451	0	···	···	···	AFM-II

552 and 596 meV/cell, respectively, than that of the ground state. The results obtained for all X-doped NiO systems are summarized in Table II and compared with those of pure NiO. The AFM-II is the magnetic ground state for all X-doped NiO systems and is the same as that of the pure NiO case. The total energy difference between the magnetic ground state and the other structures becomes small by doping s elements (Li, Na, Be, and Mg) and 3d element Zn compared with that of pure NiO, especially in the Li-doped NiO, where the energy difference is less than 200 meV/cell in the FM and AFM-I configurations. Regarding the 3d Mn and Fe dopants, the energy difference of AFM-II′ is much closer to the ground state (AFM-II), i.e., 131 and 78 meV/cell for the Mn- and Fe-doped NiO systems, respectively, than the other configurations. Larger energy differences in other magnetic configurations were found, which is a common feature for systems with X = Mn and Fe, where the total energies of FM and AFM-I are approximately 100 meV/cell higher than those of FM′ and AFM-I′ except that of FM for Fe-doped NiO.

The value of the exchange constants J_1 and J_2 for pure NiO are 0.6 and −12.2 meV, respectively, satisfying the Goodenough-Kanamori rule. Thus, the AFM-II can be stabilized by the cation-anion-cation (Ni-O-Ni) superexchange mechanism of 180° alignment ($J_2 < 0$). These values are qualitatively consistent with previous theoretical predictions [33–36] and experiments [37–39], where the J_2 is more dominant than J_1 in the system [40]. In Fig. 2, when NiO is doped with the s elements, the absolute values of both J_1 and J_2 decrease compared with those of pure NiO regarding the monovalent-cation dopants (Li^{+} and Na^{+}), whereas no changes in J_1 and J_2 are observed regarding the divalent-cation dopants (Be^{2+} and Na^{2+}). On the other hand, doping with 3d elements induces small changes in J_1 and J_2, depending on the X dopants. In Fe-doped NiO, J_1 (J_2) increases (slightly decreases) compared with that of pure NiO, whereas J_1' is larger than J_1 by 0.3 meV, and the magnitude of J_2' is significantly smaller than that of J_2 by 7.9 meV. In Mn-doped NiO, J_1 and J_2 are almost unchanged compared with those of pure NiO, but J_1' and J_2' are significantly smaller than J_1 and J_2, respectively. Changes in J_1 and J_2 are also negligible between pure and Zn-doped NiO systems.

To elucidate the trend of exchange constants J_1 and J_2, we present local density of states (DOS) in Fig. 3. Starting with pure NiO as a reference [Fig. 3(g)], where the valence-top and conduction-bottom states are composed by strong orbital hybridizations between Ni 3d and O 2p with a large band gap of approximately 4 eV, we verify that the band gap is in agreement with an experiment [41] due to the electron-electron correction ($U_{\text{eff}} = 7.52$ eV). Changes in DOS occur by doping specific elements. For the Li-doped NiO shown in Fig. 3(a), the band gap disappears, and a finite DOS is observed at the Fermi level, where the O 2p states are dominant (see inset in the figure). Since the Li^{+} is a monovalent cation and its valence number is different from that of divalent O^{2-}, electrons are transferred from the O^{2-} sites to the Li^{+} site; thus, holes are introduced into the system. It is noted that the holes are noticeable at the O^{2-} sites nearest to the Li^{+} site,

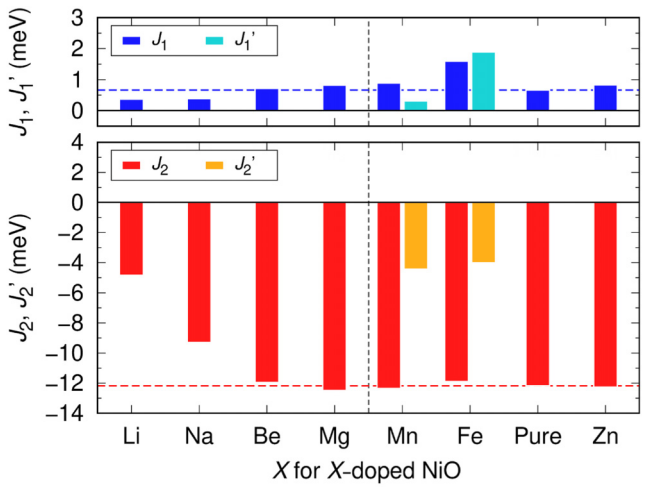

FIG. 2. (Top) Exchange constants between the first-nearest neighbor Ni-Ni (J_1; blue) and Ni-X (J_1'; skyblue) and (bottom) those between the second-nearest neighbor Ni-Ni (J_2; red) and Ni-X (J_2'; orange) for pure and X-doped NiO systems. Horizontal dashed lines represent the results of pure NiO for a reference.

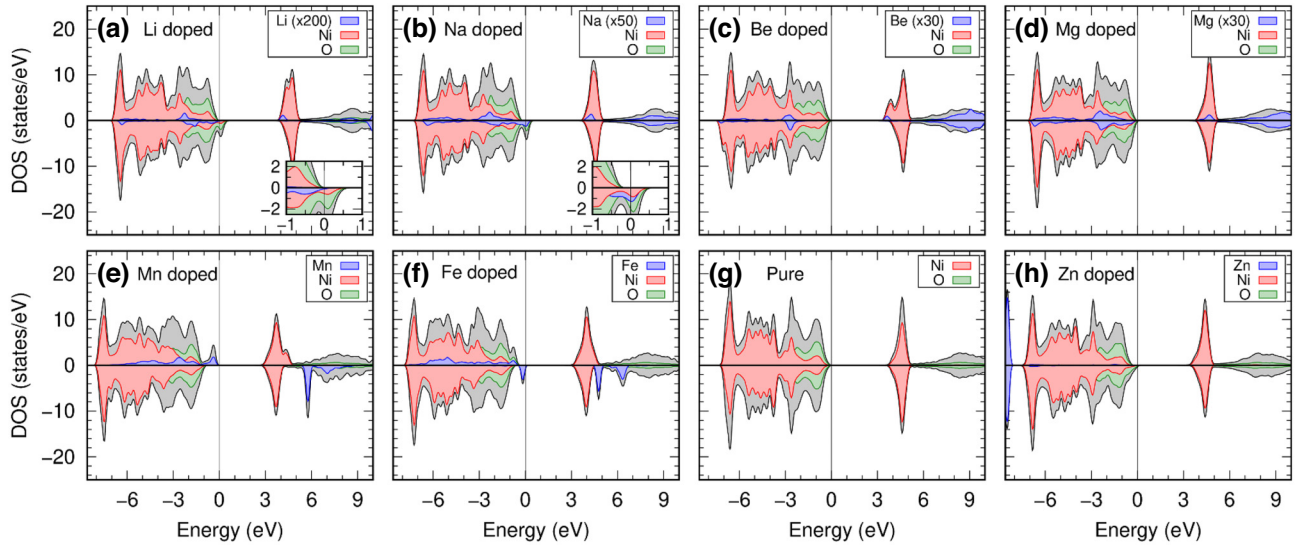

FIG. 3. Local DOS for (g) pure NiO and (a)–(f) and (h) X-doped NiO (X = Li, Na, Be, Mg, Mn, Fe, and Zn). The DOS is projected on O (green), Ni (red), and X (blue) with total DOS (gray). Positive and negative values in the vertical axes indicate DOSs in spin-up and -down states, respectively; the zero in the horizontal axes indicates Fermi level of X = Li and Na in metallic systems and the valence edge for pure NiO and X = Be, Mg, Mn, Fe, and Zn in insulator systems. The local DOSs of Ni and O are the sum of the corresponding atoms in the unit cell. Insets in (a),(b) focus around the Fermi level.

as reported in Refs. [42–44]. Accordingly, the electronic structure shows ferromagnetic character when doped with Li, and hence the absolute value of J_2 becomes apparently small compared with that of pure NiO. This mechanism holds for the Na-doped NiO. A similar reduction in J_2 can be attributed to the DOS in the ferromagnetic state [Fig. 3(b)]. On the other hand, in the other dopants (Be^{2+}, Mg^{2+}, Mn^{2+}, Fe^{2+}, and Zn^{2+}), since the ionic states are the same with that in O^{2-}, the band gap is shown in Figs. 3(c)–3(f) and 3(h), and charge transfer does not occur in these systems. Thus, J_2 is almost the same as that in pure NiO.

Next, we discuss the origin of negative J_2' between Ni and X sites in the 3d-doped systems. We initially focus on the Mn-doped NiO. Figure 4(a) illustrates an energy diagram of minority-spin 3d states of Mn and Ni via O, where t_{2g} states at the Ni site are occupied by spin-up electrons (the right side of the figure); there are no spin-down electrons at the Mn site (the left side of the figure). The majority-spin states are fully occupied (not shown in the energy diagram), and the total magnetizations at the Mn and Ni sites are represented by gray arrows in the figure. Between the Mn (d^5) and Ni (d^8) cations where the number of electrons is different, the antiferromagnetic coupling is stabilized by hybridizations between Mn t_{2g} and O 2p in the spin-down states and between Ni e_g and O 2p in the spin-up states. This leads to a more energetically favorable electronic configuration than that of electrons occupying the orbitals at the higher energy level [light-red arrows in Fig. 4(a)]. In the Fe-doped NiO shown in Fig. 4(b), only one minority-spin electron occupies t_{2g} at the Fe site, corresponding to a DOS peak of the valence top in Fig. 3(f). This minority-spin t_{2g} state is no longer degenerate due to a local Jahn-Teller distortion excited by the partial electron occupation, although in this paper, we refer to these states as t_{2g} for simplicity. Similar to the Mn-doped NiO, the antiferromagnetic coupling is stabilized by hybridizations of Fe t_{2g}–O 2p in the spin-down states and Ni e_g–O 2p in the spin-up states. A key difference between the Mn- and Fe-doped systems is that the local Jahn-Teller effect occurs in the Fe-doped NiO but not in the Mn-doped NiO. Indeed, this may reflect in the difference in magnetic anisotropy, rather than in J_2', between these systems as we will discuss in Sec. III B. Since, in the magnetic ground state of AFM-II, J_1 and J_1' do not contribute to the total energy described in Eq. (4), these exchange interactions are not discussed in this paper.

B. Magnetic anisotropy

Figure 5 shows the magnetic anisotropy energies E_{MCA}, E_{MDIA}, and E_{MA}. In the pure NiO, we obtained 0.3 μeV for the E_{MCA} with the magnetic easy axis being in the out-of-plane [111] direction, and −384 μeV for E_{MDIA} with the magnetic easy axis being in the in-plane [11$\bar{2}$] direction. The E_{MCA} value is negligible; thus, the magnetic anisotropy is mainly attributed to the MDIA, and the easy magnetization direction is along the [11$\bar{2}$]. However, this trend is drastically different in the Fe-doped NiO. A very large MCA contribution ($E_{\mathrm{MCA}} = -583$ μeV) is obtained, which is of comparable magnitude of the MDIA

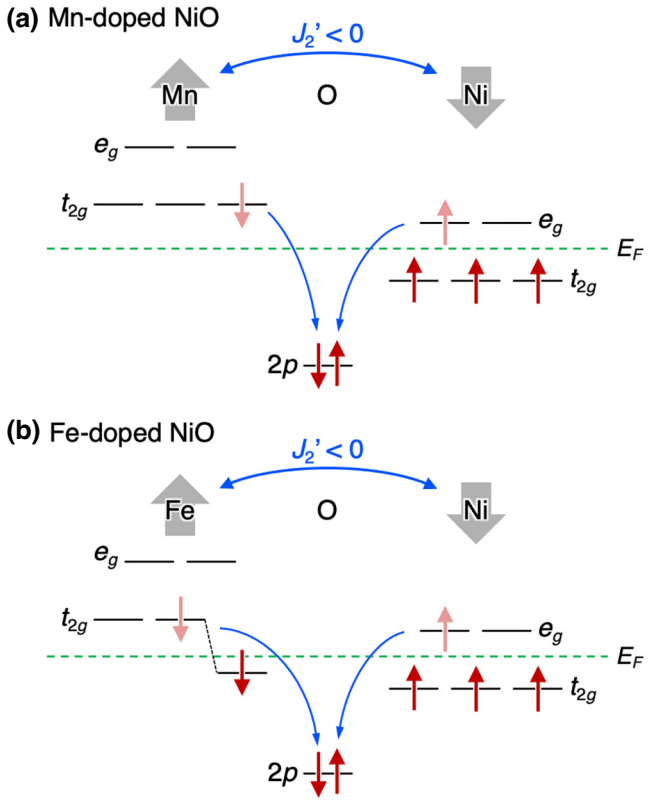

FIG. 4. Superexchange interaction mechanism between X and Ni sites (J_2') in (a) Mn-doped and (b) Fe-doped NiO systems. Energy diagram at X and Ni sites shows only minority-spin states (red arrows) and fully occupied majority-spin states are omitted for simplicity (see main text for light-red arrows), while at O site, both majority- and minority-spin states are shown. Magnetizations at X and Ni sites are shown by gray arrows above the energy diagram.

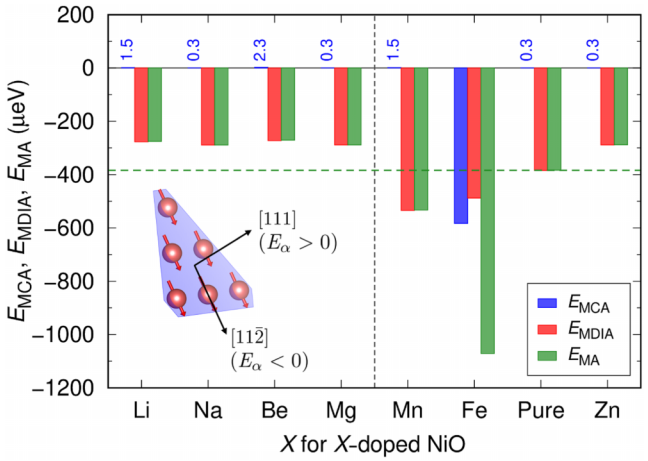

FIG. 5. E_{MCA} (blue), E_{MDIA} (red), and E_{MA} ($= E_{MCA} + E_{MDIA}$) (green) for pure and X-doped NiO systems. A positive (negative) value indicates a magnetic easy axis in the [111] ([11$\bar{2}$]) direction. The E_{MCA} (approximately 1 μeV) values are represented by blue numbers. The inset illustrates the (111) plane, where magnetization direction [11$\bar{2}$] and [111] are defined.

($E_{MDIA} = -488$ μeV); both favor [11$\bar{2}$], that is, the total value of E_{MA} is over -1000 μeV. This absolute value is the largest among the systems under study. The other X-doped NiO show that the total E_{MA} is dominated only by the E_{MDIA}, which depends on dopant X for the 3d-dopant systems, but is constant for the s-dopant systems.

In Fig. 6, a simple relation between E_{MDIA} and the local spin magnetic moment at the X site is presented. This relation is approximately linear. The Ni of pure NiO has a spin magnetic moment of 1.74 μ_B. Since the Fe and Mn have two and three electrons less than Ni, their local spin magnetic moments increase to 3.65 and 4.51 μ_B, respectively. Therefore, E_{MDIA} is enhanced by doping NiO with these cations. In contrast, since the s elements have no spontaneous magnetization (d^0) and the 3d-Zn is fully occupied ($3d^{10}$), their local spin magnetic moments are approximately zero. This means that the contribution of magnetic dipole-dipole interaction between Ni and dopant X (X = Li, Na, Be, Mg, and Zn) is small, resulting in E_{MDIA} being less dominant compared with that of the pure NiO.

To elucidate the physical origin of the large E_{MCA} in the Fe-doped NiO, we present the energy dependence in Fig. 7(a) together with the DOS for Fe and the nearest-neighbor Ni sites, where the d states are projected on the magnetic quantum number m along the [111] direction. In this analysis, the energy dependence of E_{MCA} is obtained using the torque method [45], where E_{MCA} is derived from the sum of expectation values of the angular derivative (polar angle θ and azimuthal angle ϕ) of the spin-orbit

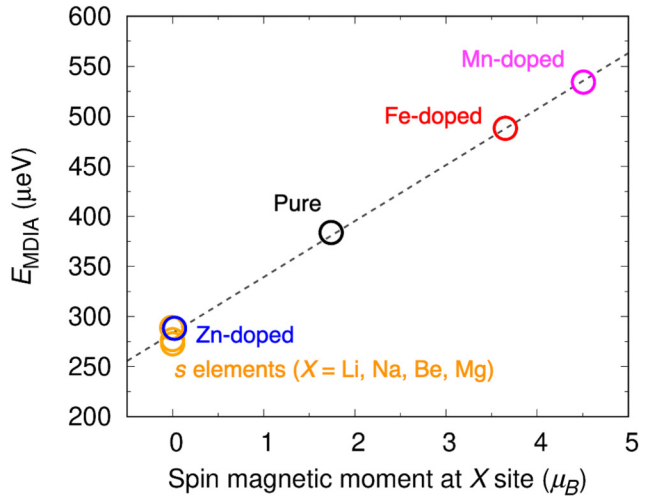

FIG. 6. Dependence of E_{MDIA} with local spin magnetic moment at X site for X-doped NiO (color circles) and pure NiO (black circle).

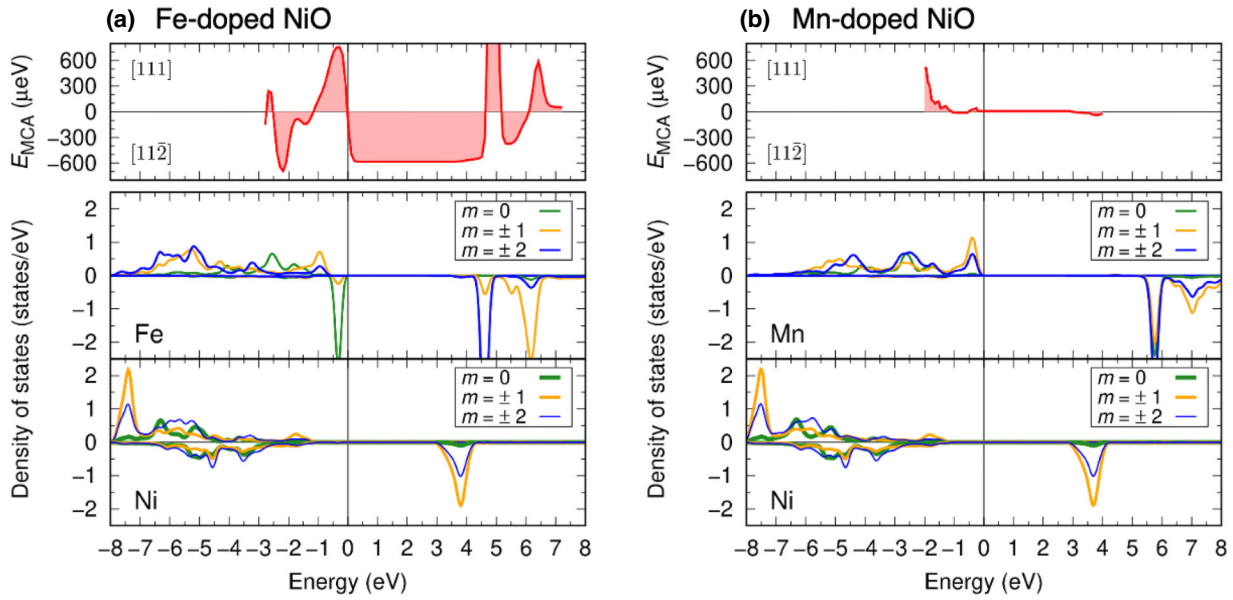

FIG. 7. Energy dependence of E_{MCA} (top) and DOS of dopant (X) and Ni sites (bottom) for (a) Fe-doped NiO and (b) Mn-doped NiO. In the DOS, the d states of X and Ni sites are projected onto $m = 0$ (green), $m = \pm 1$ (orange), and $m = \pm 2$ (blue). The Ni is at the first-nearest site from X.

coupling (SOC) Hamiltonian for all occupied electronic states.

The top panel of Fig. 7(a) shows that the energy dependence of E_{MCA} in the Fe-doped NiO is constant inside the band gap in the Fe-d DOS. At the Fe site, the band gap is composed by the valence top of $d_{m=0,\pm1}$ states (around -0.4 eV) and the conduction bottom of $d_{m=\pm1,\pm2}$ states (around 4.6 eV) in the spin-down states, whereas the electrons are fully occupied in spin-up states, as shown in the bottom panel of Fig. 7(a). Large DOS peaks of the Ni-$d_{m=\pm1,\pm2}$ states are observed at around 3.8 eV, but there is no significant change in E_{MCA} at this energy level, indicating that E_{MCA} comes from the Fe site, rather than the Ni site. According to the second-order perturbation theory analysis [46], the SOC between occupied and unoccupied states with the same (different) magnetic quantum number m couples through the $\hat{L}_z$ ($\hat{L}_x$ and $\hat{L}_y$) operator and gives rise to the magnetic easy axis preferring the out-of-plane (in-plane) direction. Specifically, it is defined as positive (negative) E_{MCA} in Eq. (5) and corresponds to the [111] ([11$\bar{2}$]) direction in this case. The SOC interaction between the occupied states of $m = 0$ ($m = \pm 1$) at the valence top and the unoccupied states of $m = \pm 1$ ($m = \pm 2$) at the conduction bottom with different m yields a negative E_{MCA}. For comparison, the results of Mn-doped NiO are shown in Fig. 7(b), confirming an almost zero E_{MCA} around the band gap (see the top panel in the figure). The spin-up states at the Mn site are fully occupied by electrons [bottom panel in Fig. 7(b)]; consequently, this half-filled state does not yield MCA.

C. Antiferromagnetic resonance frequency

Using the exchange constants and the magnetic anisotropy energy, the effective fields H_E and H_A are derived as $H_E = J/M$ and $H_A = 2K/M$ [49]. For pure NiO, it is assumed $M = |M_1| = |M_2|$ where M_i is the magnetization in sublattice i. For X-doped NiO, since the absolute value of magnetization between the Ni and X sites is different, M is obtained by averaging M_i over all sublattices in the unit cell. J is $|J_2|$ for pure NiO and X-doped NiO where X is an s element or 3d-Zn; otherwise $(18|J_2| + 6|J_2'|)/24$ for X of 3d-Mn and -Fe, where the weighting factors are obtained from the magnetic ground state of $E_{AFM\text{-}II}$, in Eq. (4). K is the effective magnetic anisotropy constant, which consists of contributions from all TM sites in the unit cell, and therefore simply treated as $|E_{MA}|$ for all systems.

The results are presented in Fig. 8. For the pure NiO, H_E is 121 T and H_A is 7.6 T, resulting in a resonance frequency $\omega_r/(2\pi) = 1.20$ THz. Doping with monovalent Li^+ leads to a large decrease in H_E (57 T), which is approximately half that of pure NiO [Fig. 8(a)] due to the large reduction in J_2 (Fig. 2). A relatively small $\omega_r/(2\pi)$ of 0.77 THz is obtained [Fig. 8(c)]. In the other dopants, H_E varies in a range of 20% from that of pure NiO. On the other hand, a large value of H_A is obtained in the Fe-doped NiO due to the large MCA contribution [skyblue in Fig. 8(b)]. As a result, $\omega_r/(2\pi)$ reaches up to 1.60 THz, which is the highest in current systems [Fig. 8(c)]. The Mn-doped NiO exhibits the largest MDIA contribution to H_A [blue in Fig. 8(b)]; however, it is less significant compared to other

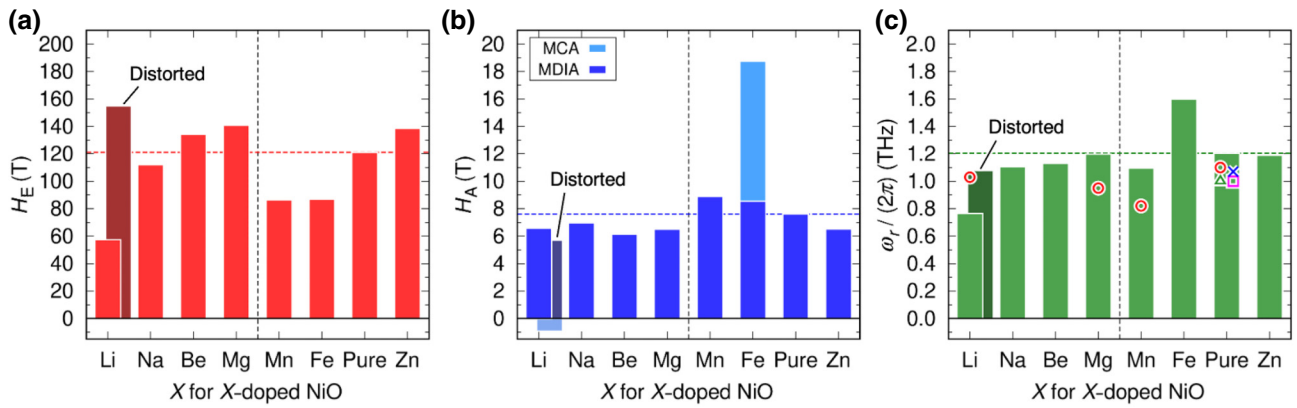

FIG. 8. (a) H_E, (b) H_A, and (c) ω_r for pure and X-doped NiO systems. The horizontal dashed lines indicate the values of pure NiO as a guide to the eye. The experimental results are plotted in (c); Ref. [16] (red circles), Ref. [20] (green triangle), Ref. [47] (magenta square), and Ref. [48] (blue cross). For cation-doped NiO [16], systems with dopant compositions close to our calculations ($Li_{0.10}Ni_{0.90}O$, $Mg_{0.08}Ni_{0.92}O$, and $Mn_{0.08}Ni_{0.92}O$) are plotted. The results for Li-doped NiO with the distortion are also presented (labeled as distorted).

contributions such as H_E and MCA in H_A. Thus, $\omega_r/(2\pi)$ is 1.18 THz, which is comparable to that of the pure NiO.

Finally, we comment on a comparison of resonance frequency with experiments [16]. Note that the same dopant composition was not available, so that we plotted the experimental data for compositions close to those of our systems, which are represented by symbols in Fig. 8(c). A quantitative agreement is observed with experimental value (1.1 THz) of the pure NiO. However, although a considerable decrease in $\omega_r/(2\pi)$ due to the cation dopants of Li, Mg, and Mn was reported in the experiment, our calculations do not follow the experimental trend. The discrepancy in the Mg- and Mn-doped NiO systems can be attributed to the fact that the doping with Mg alters the lattice constant [16], which can change the exchange constant and/or magnetizations at sublattices; also, doping with Mn causes the appearance of a second phase with $MnNi_2O_4$ spinel for a small amount of dopant ($x > 0.05$ in $Ni_{1-x}Mn_xO$), although our calculations assume a fixed lattice constant and a single RS crystal structure.

In Li-doped NiO, possible reasons for this discrepancy may related to a Jahn-Teller effect that distorts the crystal structure into lower symmetry, leading to changes in angle and length of the cation-anion bond and/or wavefunction overlapping between them. Indeed, the Jahn-Teller distortion of crystal structure significantly modifies the $\omega_r/(2\pi)$ via changes in exchange constants and magnetic anisotropy. We performed additional calculations by introducing crystal-structure distortion and by using small U_{eff} value of 5.3 eV taken from Ref. [50] (the details of distortion and U_{eff} treatment are described in the Appendix). The results are shown in Fig. 8, labeled as "distorted." The H_E is enhanced to be 155 T, which is approximately 3 times larger than that in the nondistorted system (57 T), as confirmed in Fig. 8(a). For the H_A in Fig. 8(b), the MDIA contribution is less affected by the Jahn-Teller distortion but a non-negligible MCA contribution with the opposite sign to the MDIA is obtained, thus resulting in a small value of H_A. The $\omega_r/(2\pi)$ of 1.08 THz is then obtained [Fig. 8(c)], in good agreement with the experiment [16]. These results indicate that the Jahn-Teller distortion can be an essential factor in interpreting the experimental observations, although such distortion might be so small that they cannot be clearly confirmed in the experiment.

IV. SUMMARY

We investigated the exchange constant and the magnetic anisotropy in antiferromagnetic NiO, where various

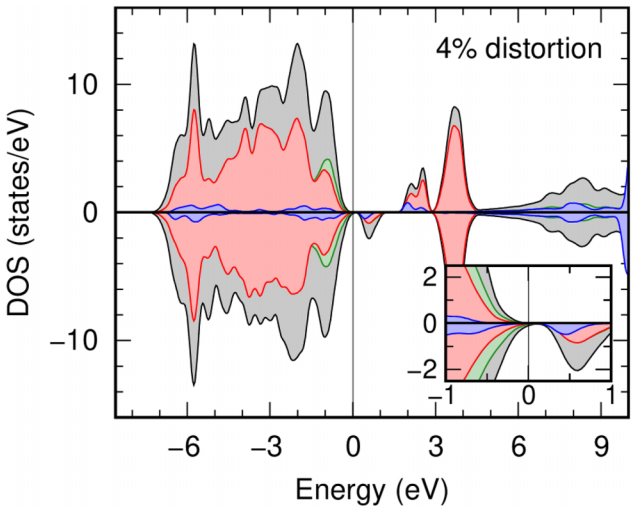

FIG. 9. Local DOS for Li-doped NiO where the crystal structure is distorted. The $U_{\text{eff}} = 5.3$ eV is used for the calculations. The notations are the same as in Fig. 3.

TABLE III. Comparison of local spin magnetic moments at Ni sites, m_{Ni} and $m_{\mathrm{Ni}'}$ (in μ_{B} unit), which are the first- and second-nearest neighbor sites from Li, exchange constants, J_1 and J_2 (in meV unit), and magnetic anisotropy energies, E_{MCA}, E_{MDIA}, and E_{MA} (in μeV unit) for Li-doped NiO in RS and distorted structures.

	m_{Ni} (μ_{B})	$m_{\mathrm{Ni}'}$ (μ_{B})	J_1 (meV)	J_2 (meV)	E_{MCA} (μeV)	E_{MDIA} (μeV)	E_{MA} (μeV)
RS	1.74	1.57	0.4	−4.8	1.5	−277	−275
Distorted	1.69	1.07	0.4	−12.6	37.7	−232	−194

cations X, including s elements (Li, Na, Be, and Mg) and $3d$ elements (Mn, Fe, and Zn), were used as dopants. We calculated the antiferromagnetic resonance frequency ω_r from first-principles calculations. The pure NiO exhibits ω_r in the THz range (1.20 THz). This value can be modulated using cation doping. The mechanism modulating ω_r through the exchange constant and the magnetic anisotropy depends on the cation dopant. Monovalent cations, especially Li^+, induce hole doping, resulting in a decreased ω_r of 0.77 THz due to the weakening of superexchange interaction in Li-doped NiO. In contrast, a large increase in ω_r is obtained using Fe cation doping, where the magnetocrystalline anisotropy preferring a magnetic easy axis in the $[11\bar{2}]$ direction plays a key role, resulting in the highest ω_r value of 1.60 THz. Using the Mn cation doping, the magnetic anisotropy caused by magnetic dipole-dipole interaction increases. However, this increase is very small, and the resultant ω_r value is comparable with that of pure NiO; hence, Mn doping is less significant regarding ω_r. Consequently, controlling the exchange constant and the magnetocrystalline anisotropy is a straightforward approach for modulating ω_r in future THz-frequency applications.

ACKNOWLEDGMENTS

Authors thank K. Miyamae and R. Ozaki for fruitful discussions. This work was partly supported by KAKENHI Grants No. JP22K14290, No. JP21K03444, No. JP21H04562, and No. JP19K03716; JST PRESTO Grant No. JPMJPR20B9; the Research Foundation for the Electrotechnology of Chubu; the Data-Science Research Center for Material, Quantum, and Measurement Technologies, Mie University; the Center for Spintronics Research Network, Osaka University; and Cooperative Research Project of the Research Institute of Electrical Communication, Tohoku University. Numerical calculations were partially performed using computational facilities at Research Institute for Information Technology, Kyushu University and at NIMS.

APPENDIX: DISTORTION AND ELECTRON-ELECTRON CORRELATION EFFECTS IN Li-DOPED NiO

The present pure and X-doped NiO systems are assumed to be in the cubic RS structure and this restriction leads to the discrepancy for the Li-doped NiO in the DOS of Fig. 3(a) with earlier calculations [50–52]. In contrast to our results in Fig. 3(a), showing the finite DOS remaining at the Fermi level due to the hole doping, the Jahn-Teller distortion that breaks the crystal structure symmetry of cubic phase induces a band gap. To take into account such Jahn-Teller distortion, we remodel our system by following the procedures of Anisimov *et al.* [51], where the lattice vectors are expanded along z axis by 4% and compressed along x and y axes by 2%. The DOS obtained for the Li-doped NiO in the distorted system is given in Fig. 9, confirming the finite band gap. Of note, in Table III, the magnetic moment at Ni site of the second-nearest neighbor from Li ($m_{\mathrm{Ni}'}$) is reduced to 1.07 μ_{B} from the case of the RS structure, 1.57 μ_{B}. This is in consistent with earlier calculation [50]. Such DOS modifies the exchange constant J_2 as increase in the magnitude from −4.8 meV (in RS) to −12.6 meV (distorted), which is reflected in the significant increase of H_{E} in Fig. 8(a). The E_{MDIA} is negligibly changed by the distortion, but the E_{MCA} is enhanced from 1.5 μeV (RS) to 37.7 μeV (distorted), which reduce the $|E_{\mathrm{MA}}|$ due to the opposite signs of E_{MCA} and E_{MDIA}. We here note that the U_{eff} value for Ni is set to 5.3 eV used in Ref. [50], this is because the use of $U_{\mathrm{eff}} = 7.52$ eV, determined from the linear-response approach [28], cannot obtain the stationary SCF solution having the band gap as in Fig. 9 in our FLAPW framework.

[1] L. Néel, Magnetism and the Local Molecular Field, Nobel Lectures, Physics 1963-1970 (1970) (1970).
[2] V. Baltz, A. Manchon, M. Tsoi, T. Moriyama, T. Ono, and Y. Tserkovnyak, Antiferromagnetic spintronics, Rev. Mod. Phys. **90**, 015001 (2018), and references therein.
[3] X. Marti, I. Fina, C. Frontera, J. Liu, P. Wadley, Q. He, R. J. Paull, J. D. Clarkson, J. Kudrnovský, I. Turek, J. Kuneš, D. Yi, J.-H. Chu, C. T. Nelson, L. You, E. Arenholz, S. Salahuddin, J. Fontcuberta, T. Jungwirth, and R. Ramesh, Room-temperature antiferromagnetic memory resistor, Nat. Mater. **13**, 367 (2014).
[4] T. Moriyama, N. Matsuzaki, K.-J. Kim, I. Suzuki, T. Taniyama, and T. Ono, Sequential write-read operations in FeRh antiferromagnetic memory, Appl. Phys. Lett. **107**, 122403 (2015).
[5] G. R. Hoogeboom, A. Aqeel, T. Kuschel, T. T. M. Palstra, and B. J. van Wees, Negative spin Hall magnetoresistance of Pt on the bulk easy-plane antiferromagnet NiO, Appl. Phys. Lett. **111**, 052409 (2017).

[6] M. Kimata, T. Moriaya, K. Oda, and T. Ono, Distinct domain reversal mechanisms in epitaxial and polycrystalline antiferromagnetic NiO films from high-field spin Hall magnetoresistance, Appl. Phys. Lett. **116**, 192402 (2020).

[7] P. Wadley *et al.*, Electrical switching of an antiferromagnet, Science **351**, 587 (2016).

[8] T. Moriyama, K. Oda, T. Ohkochi, M. Kimata, and T. Ono, Spin torque control of antiferromagnetic moments in NiO, Sci. Rep. **8**, 14167 (2018).

[9] M. Meinert, D. Graulich, and T. Matalla-Wagner, Electrical switching of antiferromagnetic Mn_2Au and the role of thermal activation, Phys. Rev. Appl. **9**, 064040 (2018).

[10] S. Y. Bodnar, L. Šmejkal, I. Turek, T. Jungwirth, O. Gomonay, J. Sinova, A. A. Sapozhnik, H.-J. Elmers, M. Kläui, and M. Jourdan, Writing and reading antiferromagnetic Mn_2Au by Néel spin-orbit torques and large anisotropic magnetoresistance, Nat. Commun. **9**, 348 (2018).

[11] J. Walowski and M. Münzenberg, Perspective: Ultrafast magnetism and THz spintronics, J. Appl. Phys. **120**, 140901 (2016).

[12] D. M. Mittleman, Perspective: Terahertz science and technology, J. Appl. Phys. **122**, 230901 (2017).

[13] K. David and H. Berndt, 6G vision and requirements: Is there any need for beyond 5G?, IEEE Veh. Technol. Mag. **13**, 72 (2018).

[14] C. Kittel, Theory of antiferromagnetic resonance, Phys. Rev. **82**, 565 (1951).

[15] T. Nagamiya, Theory of antiferromagnetism and antiferromagnetic resonance absorption, I, Prog. Theor. Phys. **6**, 342 (1951).

[16] T. Moriyama, K. Hayashi, K. Yamada, M. Shima, Y. Ohya, and T. Ono, Tailoring THz antiferromagnetic resonance of NiO by cation substitution, Phys. Rev. Mater. **4**, 074402 (2020).

[17] S. Ohkoshi, S. Kuroki, S. Sakurai, K. Matsumoto, K. Sato, and S. Sasaki, A millimeter-wave absorber based on gallium-substituted ε-iron oxide nanomagnets, Angew. Chem. Inst. Ed. **46**, 8392 (2007).

[18] A. Namai, M. Yoshikiyo, K. Yamada, S. Sakurai, T. Goto, T. Yoshida, T. Miyazaki, M. Nakajima, T. Suemoto, H. Tokoro, and S. Ohkoshi, Hard magnetic ferrite with a gigantic coercivity and high frequency millimetre wave rotation, Nat. Commun. **3**, 1035 (2012).

[19] K. Hayashi, K. Yamada, M. Shima, Y. Ohya, T. Ono, and T. Moriyama, Control of antiferromagnetic resonance and the morin temperature in cation doped α-$Fe_{2-x}M_xO_3$ (M = Al, Ru, Rh, and In), Appl. Phys. Lett. **119**, 032408 (2021).

[20] T. Moriyama, K. Hayashi, K. Yamada, M. Shima, Y. Ohya, and T. Ono, Intrinsic and extrinsic antiferromagnetic damping in NiO, Phys. Rev. Mater. **3**, 051402(R) (2019).

[21] T. Moriyama, K. Hayashi, K. Yamada, M. Shima, T. Ohya, T. Tserkovnyak, and T. Ono, Enhanced antiferromagnetic resonance linewidth in NiO/Pt and NiO/Pd, Phys. Rev. B **101**, 060402(R) (2020).

[22] L. Weymann, A. Shuvaev, A. Pimenov, A. A. Mukhin, and D. Szaller, Magnetic equivalent of electric superradiance in yttrium-iron-garnet films, Commun. Phys. **4**, 97 (2021).

[23] E. Wimmer, H. Krakauer, M. Weinert, and A. J. Freeman, Full-potential self-consistent linearized-augmented-plane-wave method for calculating the electronic structure of molecules and surfaces: O_2 molecule, Phys. Rev. B **24**, 864 (1981).

[24] M. Weinert, E. Wimmer, and A. J. Freeman, Total-energy all-electron density functional method for bulk solids and surfaces, Phys. Rev. B **26**, 4571 (1982).

[25] K. Nakamura, T. Ito, A. J. Freeman, L. Zhong, and J. F. de Castro, Enhancement of magnetocrystalline anisotropy in ferromagnetic Fe films by intra-atomic noncollinear magnetism, Phys. Rev. B **67**, 014420 (2003).

[26] J. P. Perdew, K. Burke, and M. Ernzerhof, Generalized gradient approximation made simple, Phys. Rev. Lett. **77**, 3865 (1996).

[27] A. B. Shick, A. I. Liechtenstein, and W. R. Pickett, Implementation of the LDA+U method using the full-potential linearized augmented plane-wave basis, Phys. Rev. Lett. **77**, 3865 (1996).

[28] K. Nawa, T. Akiyama, T. Ito, K. Nakamura, T. Oguchi, and M. Weinert, Scaled effective on-site Coulomb interaction in the DFT+U method for correlated materials, Phys. Rev. B **97**, 035117 (2018).

[29] R. Yu, D. Singh, and H. Krakauer, All-electron and pseudopotential force calculations using the linearized-augmented-plane-wave method, Phys. Rev. B **43**, 6411 (1991).

[30] M. Weinert, R. E. Watson, and J. W. Davenport, Total-energy differences and eigenvalues sums, Phys. Rev. B **32**, 2115 (1985).

[31] G. H. O. Daalderop, P. J. Kelly, and M. F. H. Schuurmans, First-principles calculation of the magnetocrystalline anisotropy energy of iron, cobalt, and nickel, Phys. Rev. B **41**, 11919 (1990).

[32] H. J. F. Jansen, Magnetic anisotropy in density-functional theory, Phys. Rev. B **59**, 4699 (1999).

[33] G. Fischer, M. Däne, A. Ernst, P. Bruno, M. Lüders, Z. Szotek, W. Temmerman, and W. Hergert, Exchange coupling in transition metal monoxides: Electronic structure calculations, Phys. Rev. B **80**, 014408 (2009).

[34] A. Jacobsson, B. Sanyal, M. LeÅ¿aić, and S. Blügel, Exchange parameters and adiabatic magnon energies from spin-spiral calculations, Phys. Rev. B **88**, 134427 (2013).

[35] Y. O. Kvashnin, O. Grånäs, I. Di Marco, M. I. Katsnelson, A. I. Lichtenstein, and O. Eriksson, Exchange coupling in transition metal monoxides: Electronic structure calculations, Phys. Rev. B **91**, 125133 (2015).

[36] A. Gumarilang, K. Nawa, and K. Nakamura, Role of magnetic dipole-dipole interaction on magnon in NiO, J. Phys. Soc. Jpn. **92**, 084703 (2023).

[37] M. T. Hutchings and E. J. Samuelsen, Measurement of spin-wave dispersion in NiO by inelastic neutron scattering and its relation to magnetic properties, Phys. Rev. B **6**, 3447 (1972).

[38] R. Shanker and R. A. Singh, Analysis of the exchange parameters and magnetic properties of NiO, Phys. Rev. B **7**, 5000 (1973).

[39] G. Srinivasan and M. S. Seehra, Magnetic susceptibilities, their temperature variation, and exchange constants of NiO, Phys. Rev. B **29**, 6295 (1984).

[40] Experimentally observed values of J_1 and J_2 are different from theoretical predictions [33–36], including our results, by a factor of 1/2. This is due to the definition of the Heisenberg Hamiltonian model. In the definition of experiments [37–39], $H = -\sum_{\langle i,j \rangle} J_{ij}\,\mathbf{S}_i \cdot \mathbf{S}_j$, the sum runs over all ij pairs and avoids the double counting of pair interactions, i.e., ij and ji. This is not equivalent to the definition we employed, in which the double counting is allowed. For keeping a consistency on the comparison, the sum over all the sites ($\sum_{i,j}$) is replaced by that over all the pairs ($\sum_{\langle i,j \rangle}$ or equivalently $\sum_{i>j}$) in theoretical definition, or experimental values of J_1 and J_2 are multiplied by 1/2.

[41] S. Hüfner, Electronic structure of NiO and related 3*d*-transition-metal compounds, Adv. Phys. **43**, 183 (1994).

[42] P. Kuiper, G. Kruizinga, J. Ghijsen, G. A. Sawatzky, and H. Verweij, Character of holes in $Li_xNi_{1-x}O$ and their magnetic behavior, Phys. Rev. Lett. **62**, 221 (1989).

[43] J. van Elp, H. Eskes, P. Kuiper, and G. A. Sawatzky, Electronic structure of Li-doped NiO, Phys. Rev. B **45**, 1612 (1992).

[44] J. Kuneš, V. I. Anisimov, A. V. Lukoyanov, and D. Vollhardt, Local correlations and hole doping in NiO: A dynamical mean-field study, Phys. Rev. B **75**, 165115 (2007).

[45] X. Wang, R. Wu, D.-S. Wang, and A. J. Freeman, Torque method for the theoretical determination of magnetocrystalline anisotropy, Phys. Rev. B **54**, 61 (1996).

[46] D. sheng Wang, R. Wu, and A. J. Freeman, First-principles theory of surface magnetocrystalline anisotropy and the diatomic-pair model, Phys. Rev. B **47**, 14932 (1993).

[47] T. Kampfrath, A. Sell, G. Klatt, A. Pashkin, S. Mährlein, T. Dekorsy, M. Wolf, M. Fiebig, A. Leitenstorfer, and R. Huber, Coherent terahertz control of antiferromagnetic spin waves, Nat. Photon **5**, 31 (2011).

[48] T. Satoh, S.-J. Cho, R. Iida, T. Shimura, K. Kuroda, H. Ueda, Y. Ueda, B. A. Ivanov, F. Nori, and M. Fiebig, Spin oscillations in antiferromagnetic NiO triggered by circularly polarized light, Phys. Rev. Lett. **105**, 077402 (2010).

[49] C. Kittel, *Introduction to Solid State Physics* (John Wiley & Sons, New York, 2004), 8th ed.

[50] H. Chen and J. H. Harding, Nature of the holes states in Li-doped NiO, Phys. Rev. B **85**, 115127 (2012).

[51] V. I. Anisimov, J. Zaanen, and O. K. Andersen, Band theory of Mott insulators: Hubbard U instead of Stoner I, Phys. Rev. B **44**, 943 (1991).

[52] F. Wrobel, H. Park, C. Sohn, H.-W. Hsiao, J.-M. Zuo, H. Shin, H. N. Lee, P. Ganesh, A. Benali, P. R. C. Kent, O. Heinonen, and A. Bhattacharya, Doped NiO: The Mottness of a charge transfer insulator, Phys. Rev. B **101**, 195128 (2020).